Chinese Journal of
POLYMER SCIENCE

RESEARCH ARTICLE

https://doi.org/10.1007/s10118-026-3710-x
Chinese J. Polym. Sci.

Energy Storage Performance of Supercapacitors with Polyelectrolyte Surface Coatings: Effects of Dielectric Contrast

Yi-Yao Han, Ming-Yu Chen, and Xiao-Fei Xu*

State Key Laboratory of Chemical Engineering and School of Chemical Engineering, East China University of Science and Technology, Shanghai 200237, China

Electronic Supplementary Information

Abstract The interfacial structure at the electrode-electrolyte interface is a critical determinant of the performance of electrochemical supercapacitors. Although grafting polyelectrolyte (PE) brushes onto electrodes is a promising strategy to enhance charge storage, the role of dielectric contrast and its coupling with PE microstructure remains to be studied. In this work, a classical density functional theory (cDFT) is employed to elucidate the synergistic effects of dielectric contrast and PE microstructure on supercapacitor performance. The theory explicitly accounts for image-charge interaction induced by dielectric discontinuity, chain correlation of the PE, excluded volume effect, and electrostatic correlation. The results reveal that increasing the grafting density and chain length of the PE brushes significantly enhances the capacitance by providing more immobile charge sites and expanding the effective double-layer region, which facilitates stronger counterion adsorption. It is found that the dielectric contrast between the electrode substrate and solvent, which is often oversimplified in idealized models, plays a decisive role. A higher dielectric permittivity of the substrate weakens the shielding effect of the polarization field within the electrode. Consequently, the external electric field provides a stronger influence on the electrolyte, promoting a denser accumulation of counterions at the interface. Crucially, a high-dielectric substrate mitigates the repulsive image-charge interaction, effectively transforming it into an attractive force that further adsorbs charge near the electrode. This effect becomes particularly pronounced at high surface potentials. These results provide fundamental insights into the optimization of high-performance SCs using PE coatings.

Keywords Classical density functional theory; Polyelectrolyte brushes; Dielectric contrast; Image-charge interaction; Supercapacitors

Citation: Han, Y. Y.; Chen, M. Y.; Xu, X. F. Energy storage performance of supercapacitors with polyelectrolyte surface coatings: effects of dielectric contrast. *Chinese J. Polym. Sci.* https://doi.org/10.1007/s10118-026-3710-x

INTRODUCTION

Supercapacitors (SCs) have received widespread attention as important energy storage devices.[1] Electrodes of SCs are usually made of porous materials[2] to greatly increase the energy storage. The performance of SCs can be further modulated by grafting polyelectrolyte (PE) onto the electrode surface.[3] The conducting solid phase and the electrolyte phase typically have different dielectric permittivities,[4] which results in a highly spatially non-uniform local dielectric environment.[5,6] The energy storage performance is greatly affected by the dielectric contrast, which not only changes the structure of the electric double layer, but also regulates the electrostatic screening length scale, ion solvation/desolvation behavior, and particle transport properties.[7,8] It is important to study these properties under the dielectric contrast effect, which provides important insights into the rational design for high-performance SCs.

Experimental studies have demonstrated that PE coatings can systematically alter the electrochemical properties of porous electrodes,[9] with improved capacitance,[10] ion enrichment near the electrodes,[11] and cyclic charging/discharging stability.[12,13] It is difficult to study the dielectric contrast effect on the energy storage performance by experimental methods directly, because it is coupled with surface and molecular interactions.[14] It remains unclear how the dielectric contrast quantitatively affects the EDL structure and energy storage performance of SCs. There is an urgent need to develop theoretical modeling with controllable parameters to independently quantify the dielectric properties.

Simulation and theoretical studies have provided important insights into how dielectric contrast can reconfigure the electrostatic properties near the electrodes.[15] In the model using an implicit solvent, the dielectric contrast induces image charge effect,[16] which alters the local electrostatic environment, affecting the energy storage performance of SCs. At conducting surface,[17] the image charges typically exert an attractive force on the counterions, promoting counterions accumulation, which can apparently increase capacitance and accelerate the charging dynamics. In contrast, at insulating surface,[18] the image charges exert repulsive force on the counterions, yielding ion depletion and reduced local charge storage. In many cases,[19] the charged particles are often described by the point-charge model,[20,21] thus underestimat-

* Corresponding author, E-mail: xuxf@ecust.edu.cn
Received February 25, 2026; Accepted April 8, 2026; Published online July 20, 2026

ing the image charge interaction and the associated interactions.[22]

PE brushes have been extensively investigated as functional interfacial layers capable of regulating ion distributions and electrostatic interactions.[23–25] Classical scaling theories and self-consistent field approaches have established that the structure of PE brushes is governed by the competition between chain elasticity, excluded volume interaction, and electrostatic repulsion.[26] Subsequent theoretical and simulation studies have shown that brush height, counterion confinement, and osmotic pressure strongly depend on grafting density, chain length, and ionic strength.[27] In electrochemical systems, PE brushes are particularly important because their charged segments directly interact with mobile ions and external electric fields, enabling tunable electric double-layer structure and responsive interfacial properties.[28,29] Despite these advances, prior theoretical and simulation studies of PE-grafted electrodes often rely on different levels of approximation. It is necessary to systematically examine the effects at different levels within a unified framework.[30,31]

The energy storage performance of SCs with PE coatings is influenced by factors including PE grafting conditions,[28] electrolyte species and concentration,[32,33] solvent,[34] surface structure and interactions.[35] It is important to consider all of these factors simultaneously. Classical density-functional theory (cDFT) provides a valuable alternative to describe this system, where the free energy is expressed as a functional of density profiles, taking these factors into account simultaneously and self-consistently. Recently, a free-energy functional was proposed to describe the dielectric contrast, image-charge and ion solvation effects.[36] cDFT using this free-energy functional offers good predictions on the PE coating layer,[37] which can be further extended to study the energy storage performance of PE-coated SCs.

Compared with earlier studies, the present work employs a theoretical framework that simultaneously incorporates dielectric discontinuity, image-charge interaction, and PE chain connectivity in a consistent manner. This enables a systematic investigation of the coupled effects of interfacial polarization and brush microstructure on electric double-layer structure and capacitance, which has not been fully addressed in previous studies. This work studies the dielectric contrast effect on the energy storage performance of PE-coated SCs by cDFT, considering influences of temperature, PE grafting conditions and pore width. The relationship between surface/interface microstructure and energy storage performance in the presence of dielectric contrast is obtained. It is found that the grafting conditions and the change of substrate dielectric permittivity significantly affect the energy storage performance of SCs. These results provide useful guidance for the rational design of high-performance SCs.

MODEL AND THEORY

Molecular Model

The schematics of the system are shown in Fig. 1. The electrodes in the SCs are composed of porous carbon-based materials. The capacitive properties can be enhanced by coating a layer of PE chains on the pore surface.[38,39] The schematic of one slit-like pore is shown in the right side in Fig. 1, which is the system studied in this work. The pore width is L, which is defined as the separation distance between the two parallel electrode surfaces along the z-direction. Both pore surfaces are grafted uniformly with polyion chains that are in contact with the electrolyte solution. The dielectric permittivities for solvent and substrate material are $\varepsilon_s = \varepsilon_0\varepsilon_s^r$ and $\varepsilon_p = \varepsilon_0\varepsilon_p^r$, respectively, where ε_0 is the vacuum permittivity. ε_s^r and ε_p^r represent the relative dielectric permittivities of the solvent and substrate, respective-

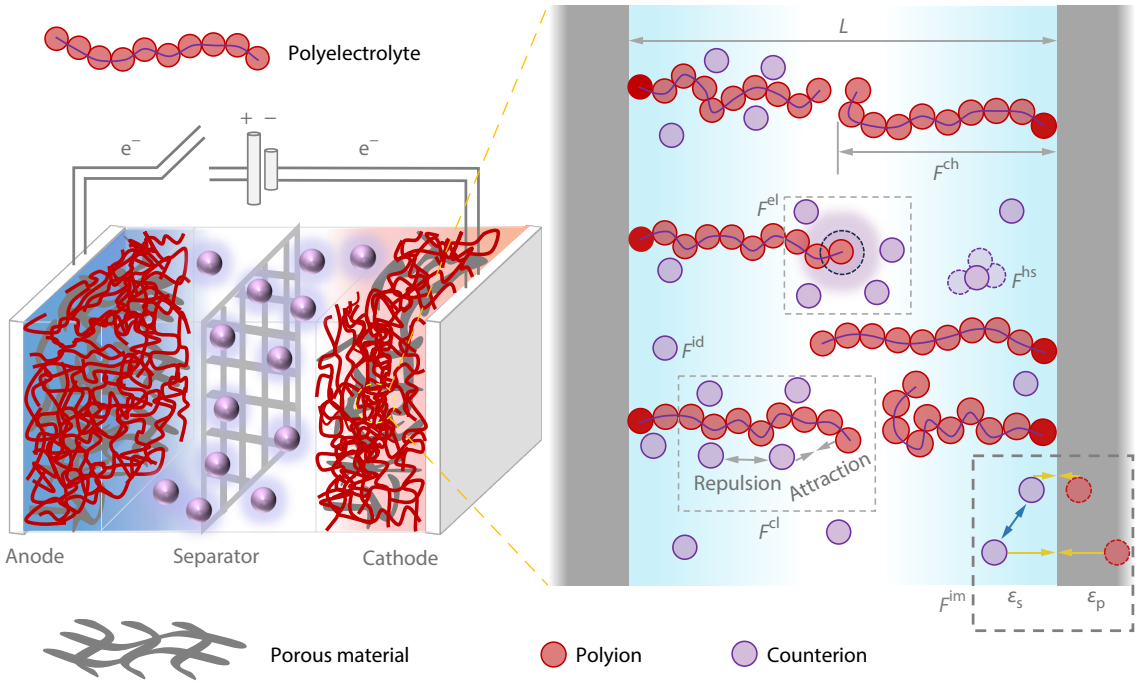

Fig. 1 Schematic illustration of porous PE-grafted SC.

https://doi.org/10.1007/s10118-026-3710-x

ly.

The two surfaces of the slit are set to the same electric potential (ψ_s). There are two explicit species in the solution: PE (indexed by 1) and counterion (indexed by 2). The PE chains are modeled as linear and freely-jointed chains, which are grafted evenly on the surface. The chain length is N. The chain length N denotes the number of segments in one polyelectrolyte chain. The grafted segment is neutral, while all the other segments carry the same charge $q_1 e_0$, where e_0 represents the elementary charge and q_1 is the charge valency ($q_1 = -1$). The counterions are modeled as positively-charged spheres with charge $q_2 e_0$ and $q_2 = +1$. For simplicity, the PE segments and counterions are assumed to have the same diameter ($\sigma = 0.4$ nm). The temperature is set at 298 K.

The pair interaction between any two beads (PE segment or counterion) is given by

$$u(r) = \begin{cases} \infty, & r < \sigma \\ k_B T l_B \dfrac{q_i q_j}{r}, & r \geq \sigma \end{cases} \tag{1}$$

where r is the distance between the two beads, k_B is the Boltzmann constant, and $l_B = e_0^2/(4\pi\varepsilon_s k_B T)$ is the Bjerrum length. The surface interacts with beads *via* the potential of

$$V_i^{ext}(z) = \begin{cases} \infty, & z < \dfrac{\sigma}{2} \\ 0, & z \geq \dfrac{\sigma}{2} \end{cases} \tag{2}$$

where the z-axis is perpendicular to the surface.

Theory

The system is described using cDFT.[40,41] For convenience, the equations in the following text are written by using the scaled parameters of $\chi \equiv \varepsilon k_B T/e_0^2$ and $\psi \equiv \phi e_0/(k_B T)$, where ε is the permittivity and ϕ is the electrostatic potential. The Helmholtz free energy includes several items, which describes different interactions or effects in the mixture.[42,43] Herein, it consists of

$$F = F^{id} + F^{hs} + F^{ch} + F^{el} + F^{cl} + F^{im} \tag{3}$$

where F^{id} describes the translational and configurational entropy of mobile ions and PE chains.[44] It is given by

$$\beta F^{id}[\{\rho_i(\boldsymbol{r})\}] = \int d\boldsymbol{R}\rho_N(\boldsymbol{R})[\ln\rho_N(\boldsymbol{R}) - 1] + \beta\int d\boldsymbol{R}\rho_N(\boldsymbol{R})V_B(\boldsymbol{R}) + \int d\boldsymbol{r}\rho_2(\boldsymbol{r})[\ln\rho_2(\boldsymbol{r}) - 1] \tag{4}$$

where $\beta = (k_B T)^{-1}$ is the Boltzmann inverse. $\boldsymbol{R} = (\boldsymbol{r}_1, \boldsymbol{r}_2, \cdots, \boldsymbol{r}_N)$ is the chain-conformation vector, and $\boldsymbol{r}_i$ is the position vector of i^{th} bead. N is the chain length. $\rho_N(\boldsymbol{R})$ is the multi-dimensional density of polymer chains. $\rho_2(\boldsymbol{r})$ is the density of the counterion. V_B is the potential for describing the chemical bonding. The total bonding potential of the linear chain is given by[45]

$$\exp[-\beta V_B(\boldsymbol{R})] = l\prod_{i=2}^{N}\frac{\delta(|\boldsymbol{r}_i - \boldsymbol{r}_{i-1}| - \sigma)}{4\pi\sigma^2} \tag{5}$$

where δ is the Dirac function and the constant l is determined by the normalized condition of mass conservation, *i.e.*

$$\frac{1}{N}\int \rho_1(\boldsymbol{r})\,d\boldsymbol{r} = \rho_g \tag{6}$$

where ρ_g is the surface-grafting density. The total density of PE segments $\rho_1(\boldsymbol{r})$ is related to the chain density *via*

$$\rho_1(\boldsymbol{r}) = \sum_{i=1}^{N}\rho_{seg,i}(\boldsymbol{r}) = \sum_{i=1}^{N}\int \rho_N(\boldsymbol{R})\delta(\boldsymbol{r} - \boldsymbol{r}_i)\,d\boldsymbol{r}_i \tag{7}$$

where $\rho_{seg,i}(\boldsymbol{r})$ is the density distribution of i^{th} segment.

The term F^{hs} describes the excluded volume effect of hard core.[46–48] Following the modified fundamental measure theory, there is

$$\beta F^{hs}[\{\rho_i(\boldsymbol{r})\}] = \int f^{hs}[\{\rho_i(\boldsymbol{r})\}]\,d\boldsymbol{r} \tag{8}$$

with

$$f^{hs}[\{\rho_i(\boldsymbol{r})\}] = -n_0\ln(1 - n_3) + \frac{n_1 n_2 - \boldsymbol{n}_{V1}\cdot\boldsymbol{n}_{V2}}{(1 - n_3)^2} + \frac{1}{36\pi}\left[n_3\ln(1 - n_3) + \frac{n_3^2}{(1 - n_3)^2}\right]\frac{\left(n_2^3 - 3n_2\boldsymbol{n}_{V2}\cdot\boldsymbol{n}_{V2}\right)}{n_3^3} \tag{9}$$

$\{n_\alpha | \alpha = 0,1,2,3,V1,V2\}$ is the Rosenfeld's functional. For multi-component system, there is $n_\alpha = \sum_i n_{\alpha i}$, where $n_{\alpha i}$ is the functional for species i. $n_{\alpha i}$ is given by following two equations:

$$\begin{cases} n_{2i}(\boldsymbol{r}) = \int d\boldsymbol{r}'\rho_i(\boldsymbol{r}')\delta\left(\dfrac{\sigma_i}{2} - |\boldsymbol{r} - \boldsymbol{r}'|\right) \\ n_{3i}(\boldsymbol{r}) = \int d\boldsymbol{r}'\rho_i(\boldsymbol{r}')\Theta\left(\dfrac{\sigma_i}{2} - |\boldsymbol{r} - \boldsymbol{r}'|\right) \\ \boldsymbol{n}_{V2,i}(\boldsymbol{r}) = \int d\boldsymbol{r}'\rho_i(\boldsymbol{r}')\Theta\left(\dfrac{\sigma_i}{2} - |\boldsymbol{r} - \boldsymbol{r}'|\right)\dfrac{\boldsymbol{r} - \boldsymbol{r}'}{|\boldsymbol{r} - \boldsymbol{r}'|} \end{cases} \tag{10}$$

and

$$n_{0i}(\boldsymbol{r}) = \frac{n_{2i}(\boldsymbol{r})}{\pi\sigma_i^2}, n_{1i}(\boldsymbol{r}) = \frac{n_{2i}(\boldsymbol{r})}{2\pi\sigma_i}, \boldsymbol{n}_{V1i}(\boldsymbol{r}) = \frac{\boldsymbol{n}_{V2i}(\boldsymbol{r})}{2\pi\sigma_i} \tag{11}$$

where Θ is the Heaviside step function, σ_i is the bead diameter of specie i.

The term F^{ch} describes the correlation effect of chain connectivity,[36,49–51] which accounts for the free energy difference between the states of connected and disconnected spheres. Using the first-order thermodynamic perturbation theory (TPT1),[52,53] there is

$$\beta F^{ch}[\{\rho_i(\boldsymbol{r})\}] = \left(\frac{1}{N} - 1\right)\int f^{ch}[\{\rho_i(\boldsymbol{r})\}]\,d\boldsymbol{r} \tag{12}$$

with

$$f^{ch} = n_{01}(\boldsymbol{r})\ln y_1[\{\rho_i(\boldsymbol{r})\}] \tag{13}$$

and

$$y_1 = \left[\frac{1}{1 - n_3} + \frac{n_2\sigma_1}{4(1 - n_3)^2}\right]\exp\left\{\left[q_1^2 - \left(q_1^{eff}\right)^2\right]\frac{l_B}{\sigma_1}\right\} \tag{14}$$

where q_1 is the charge valency of PE segments, and q_1^{eff} is the effective charge due to the charge correlation effect.

The electrostatic correlation term F^{el} refers to the interaction between charged particles. For charged spheres, F^{el} also accounts for the entropy effect of ion solvation.[49] From the mean-spherical approximation (MSA),[54–57] the functional expression of F^{el} can be obtained by using the Rosenfeld's functional, given by

$$\beta F^{el}[\{\rho_i(\boldsymbol{r})\}] = \int d\boldsymbol{r} f^{el}[\{\rho_i(\boldsymbol{r})\}] \tag{15}$$

with

$$f^{el} = l_B\sum_i n_{0i}(\boldsymbol{r})\left(\frac{q_i q_i^{eff}(\boldsymbol{r})}{\sigma_i} - \frac{q_i^2}{\sigma_i}\right) + \frac{1}{3\pi}\Gamma^3(\boldsymbol{r}) \tag{16}$$

The effective charge valency is

$$q_i^{\text{eff}}(\boldsymbol{r}) = \frac{q_i - P(\boldsymbol{r})\sigma_i^2}{1 + \Gamma(\boldsymbol{r})\sigma_i} \tag{17}$$

Γ and P can be solved consistently by the following equations:

$$\begin{cases} \Gamma^2(\boldsymbol{r}) = \pi l_B \sum_i n_{0i} \left(q_i^{\text{eff}}\right)^2 \\ P(\boldsymbol{r}) = \frac{4}{\pi}\sum_i \frac{n_{1i}q_i}{1+\Gamma\sigma_i}\left[1 - n_3 + 3\sum_i \frac{n_{3i}}{1+\Gamma\sigma_i}\right]^{-1} \end{cases} \tag{18}$$

For point charges, the first item in Eq. (16) reduces to the Born energy. The second item in Eq. (16) just describes the entropic effect due to charge correlation. Eqs. (14)–(16) are constructed from the free energy expressions in bulk phase from MSA. When the density distributions are uniform, *i.e.*, $\rho_i(r) = \rho_i^{\text{b}}$, the expressions just reduce to the free energy expression in MSA.

The Coulombic interaction term F^{cl} is the contribution of electrostatic potential (ψ), which arises from the direct Coulombic interaction,[58,59] given by

$$\beta F^{\text{cl}}[\{\rho_i(\boldsymbol{r})\}] = \int d\boldsymbol{r}\left[\sum_i \psi(\boldsymbol{r}) q_i \rho_i(\boldsymbol{r}) - \frac{1}{2}\chi_s|\nabla\psi(\boldsymbol{r})|^2\right] \tag{19}$$

In order to describe the image charge effect, the electrostatic potential is solved by the modified Poisson-Boltzmann equation of[60,61]

$$-\nabla\cdot(\chi\nabla\psi) = \sum_i \lambda_i q_i \exp(-q_i\psi - u_i) \tag{20}$$

with the boundary conditions

$$\psi(0) = \psi_s, \psi(L) = \psi_s \tag{21}$$

The boundary conditions indicate that the two surfaces of slit pore have the same electric potential ψ_s. This enforces each wall to be at the same ψ_s, which is consistent with the situation of porous carbon electrodes in the circuit. $\lambda_i = \overline{\rho}_i \exp[-q_i^2\overline{\kappa}/(8\pi\chi_s)]$, where $\overline{\rho}_i$ is the average density of species i in the simulation box. $\overline{\kappa} = (\sum_i q_i^2\overline{\rho}_i/\chi_s)^{1/2}$ is the average value of the inverse of the screening length. It should be emphasized that the dielectric discontinuity between the electrode substrate and the electrolyte is explicitly taken into account through the parameter χ in Eq. (20). The χ-parameter is also position-dependent. If the distribution is only z-dependent, it is given by

$$\chi(z) = \begin{cases} \chi_s, z > 0 \\ \chi_p, z = 0 \end{cases} \tag{22}$$

where $\chi_s = \varepsilon_s k_B T/e_0^2$ and $\chi_p = \varepsilon_p k_B T/e_0^2$.

u_i is the self-energy of species i, referring to the energy related to the interaction between the ion and the solvent. Near the surface, due to the existence of dielectric contrast, self-energy is position-dependent. Assuming that the density distribution only depends on the z-axis, there is[62]

$$u_i(z) = \frac{q_i^2}{8\pi\chi_s}[-\kappa(z) + J(z;\kappa(z))] \tag{23}$$

where

$$J(z;\kappa(z)) = 2\sum_{m=2,4,6,\ldots}\frac{(\Delta\varepsilon)^m e^{-mL\kappa(z)}}{mL} + \sum_{m=1,3,5}(\Delta\varepsilon)^m\left[\frac{e^{-(mL+2z)\kappa(z)}}{mL+2z} + \frac{e^{-(mL-2z)\kappa(z)}}{mL-2z}\right] \tag{24}$$

In the numerical calculation, the series is summed up to $m = 10$. $\Delta\varepsilon = (\varepsilon_s - \varepsilon_p)/(\varepsilon_s + \varepsilon_p)$ is the dielectric contrast. The first item in the expression of self-energy u_i describes the entropic effect of ionic strength, while the second item describes the image charge effect caused by the dielectric contrast. In this way, the image charge effect is fully incorporated into the self-energy. $\kappa(z)$ is the inverse of the local screening length, given by

$$\kappa(z) = \left(\frac{1}{\chi_s}\sum_i q_i^2\rho_i(z)\right)^{1/2} \tag{25}$$

The free energy of the image charge effect is calculated by the integral equation of the z variable over the entire system, and the expression is[36,63]

$$F^{\text{im}} = \int d\boldsymbol{r} f^{\text{im}}(\boldsymbol{r}) \tag{26}$$

Since the density distribution is only related to z, the integrand is given by the following equation[36,37]

$$f^{\text{im}}(z) = \frac{\kappa^2(z)}{8\pi z}\Delta\varepsilon\int_0^1 ds s\exp[-2s\kappa(z)z] \tag{27}$$

It should be pointed out that the calculations fully account for image charge effects of all components in the system, although the image charges of PE chains are not depicted in Fig. 1.

Finally, the grand potential W is a functional of density distribution $\rho_i(\boldsymbol{r})$ with PE and counterion, given by

$$W[\{\rho_i(\boldsymbol{r})\}] = F + \sum_i \int d\boldsymbol{r}\rho_i(\boldsymbol{r})\left[V_i^{\text{ext}}(\boldsymbol{r}) - \mu_i\right] \tag{28}$$

where μ_i denotes the chemical potential. Minimization of the grand potential to the density distributions,

$$\frac{\delta W}{\delta\rho_i(\boldsymbol{r})} = 0 \tag{29}$$

gives the control equations at the equilibrium state.[64]

The control equations in one-dimensional case are[51]

$$\begin{cases} \rho_1(z) = \sum_{i=1}^N \exp[\beta(\mu_1 - \zeta_{1,i}(z))] G_i^L(z) G_i^R(z) \\ \rho_2(z) = \exp[\beta(\mu_2 - \zeta_2(z))] \end{cases} \tag{30}$$

The subscript 1, i refers to the i^{th} segment in the PE chain. The effective fields ζ are given as follows

$$\begin{cases} \beta\zeta_{1,i}(z) = \beta V_{1,i}^{\text{ext}}(z) + q_1\psi(z) + \beta\frac{\delta g}{\delta\rho_{1,i}(z)}, i = 1,2,\ldots,N \\ \beta\zeta_2(z) = \beta V_2^{\text{ext}}(z) + q_2\psi(z) + \beta\frac{\delta g}{\delta\rho_2(z)} \end{cases} \tag{31}$$

where $g = f_{\text{hc}} + f_{\text{el}} + f_{\text{im}}$, is the sum of three free energy densities. The left and right Green propagators are calculated from the recursive relation

$$\begin{cases} G_i^L(z) = \frac{1}{2\sigma}\int_{-\sigma}^{\sigma} dz_1 \exp[-\beta\zeta_{1,i-1}(z+z_1)] G_{i-1}^L(z+z_1) \\ G_i^R(z) = \frac{1}{2\sigma}\int_{-\sigma}^{\sigma} dz_1 \exp[-\beta\zeta_{1,i+1}(z+z_1)] G_{i+1}^R(z+z_1) \end{cases} \tag{32}$$

with

$$G_N^R = 1, G_1^L(z) = \rho_g\delta\left(z - \frac{\sigma}{2}\right) \tag{33}$$

The flow scheme for cDFT at PE-grafted SC is shown in Fig. 2. The calculation procedure is as follows. The mesh grid size in z-direction is $\Delta z = 0.02\sigma$. The density profiles are calculat-

ed by Eq. (30) using the Picard iteration with a relaxation factor of 0.001. The electric potential distribution is updated at every iteration step, which is solved from the modified Poisson-Boltzmann equation Eq. (20) with boundary conditions of Eq. (21). In the limiting case (u_i = 0), Eq. (20) just reduces to the standard Poisson-Boltzmann equation. The density profiles at equilibrium are obtained when the differences between two successive iteration steps satisfy the convergence condition of $\left|\left|\rho_i^{(n+1)}(z) - \rho_i^{(n)}(z)\right|\right| < 10^{-8}$. Because of this high convergence condition, the numerical calculations of electrostatic potential (Eq. 20) and density distributions (Eq. 30) are self-consistent at low grafting densities (lower than 0.0625 nm^{-2}). It means that the electrostatic potential calculated by Eq. (20) is an alternative to describe the self-energy contribution. However, at a high grafting density and low surface potential, the λ_i should be position-dependent, and take the other contributions (excluded-volume effect, chain correlation, *etc.*) into account. In that case, Eqs. (20) and (30) would be self-consistent in theory.

It should be mentioned that the density profiles in three-dimensional description depend on the *x*, *y* and *z* directions. The density profiles $\rho_i(z)$ reported in this work correspond to averages over the *x* and *y* directions. In this sense, lateral inhomogeneities in the *x*-*y* plane are integrated out, yielding effective one-dimensional profiles $\rho_i(z)$. More numerical details can be found in relevant references.[46,51,65,66]

RESULTS AND DISCUSSION

In this work, polarizable surfaces and non-polarizable surfaces are referred to as PS and NPS, respectively. For NPS, the self-energy term u_i is set to zero. More explanations are explained in Table 1. It should be pointed out that perfect conductor (infinite ε_p) is not a PS. However, for the sake of convenience in narration, the case of $u_i \neq 0$ for any ε_p is named as PS in this work.

The charging/discharging properties can be described by the curves of surface charge density (Q_s) versus surface potential (ψ_s), which are shown in Fig. 3. At given ψ_s, the electric potential distribution $\psi(z)$ is solved from the modified PB equation. Consider a small surface area *A* on the electrode. Draw a small cylinder that straddles the surface, with its top face just above the surface and its bottom face just below. Let the thickness of the cylinder be h_c. Gaussian law states that the net electric flux through any closed surface is proportional to the enclosed charge, *i.e.*,

$$\oint_S E \cdot \mathrm{d}\boldsymbol{A} = \frac{Q_s A}{\varepsilon_s} \tag{34}$$

As the thickness of the cylinder approaches zero, the flux through the cylinder sides becomes negligible. As a result, only the flux through the top and bottom faces remains, *i.e.*,

$$(\boldsymbol{E}_{\text{above}} \cdot \boldsymbol{n})\, A - (\boldsymbol{E}_{\text{below}} \cdot \boldsymbol{n})\, A = \frac{Q_s A}{\varepsilon_s} \tag{35}$$

where $\boldsymbol{n}$ is the unit normal vector. Then, there is[67]

$$E_{\text{above},n} - E_{\text{below},n} = \frac{Q_s}{\varepsilon_s} \tag{36}$$

where $E_{\text{above},n}$ and $E_{\text{below},n}$ are the normal components of the electric field. Using the definition of electric potential $E = -\nabla\psi$, there is

$$\frac{\mathrm{d}\psi_{\text{above}}}{\mathrm{d}z} - \frac{\mathrm{d}\psi_{\text{below}}}{\mathrm{d}z} = -\frac{Q_s}{\varepsilon_s} \tag{37}$$

When the electric field inside the electrode is zero, there is

$$\psi'(0) \equiv \frac{d\psi_{\text{above}}}{\mathrm{d}z} = -\frac{Q_s}{\varepsilon_s} \tag{38}$$

This equation is used to calculate the surface charge. It

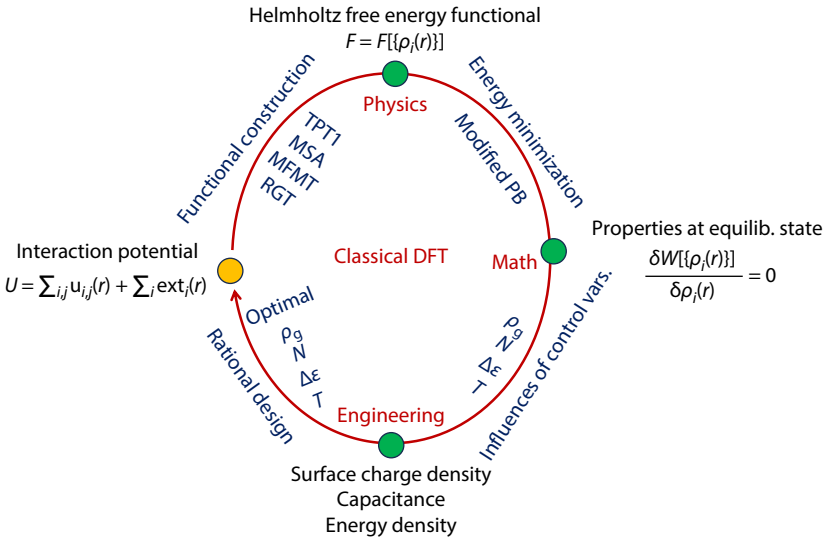

Fig. 2 Flow scheme for the application of cDFT in predicting the energy storage performance of SCs.

Table 1 Cases considered in this work.

Nomenclature	Full-spelling	Self-energy	Dielectric contrast
PS	Polarizable surface	$u_i \neq 0$	$\Delta\varepsilon \neq 0$ in most cases, but $\Delta\varepsilon = 0$ is possible
NPS	Non-polarizable surface	$u_i = 0$	$\Delta\varepsilon = 0$

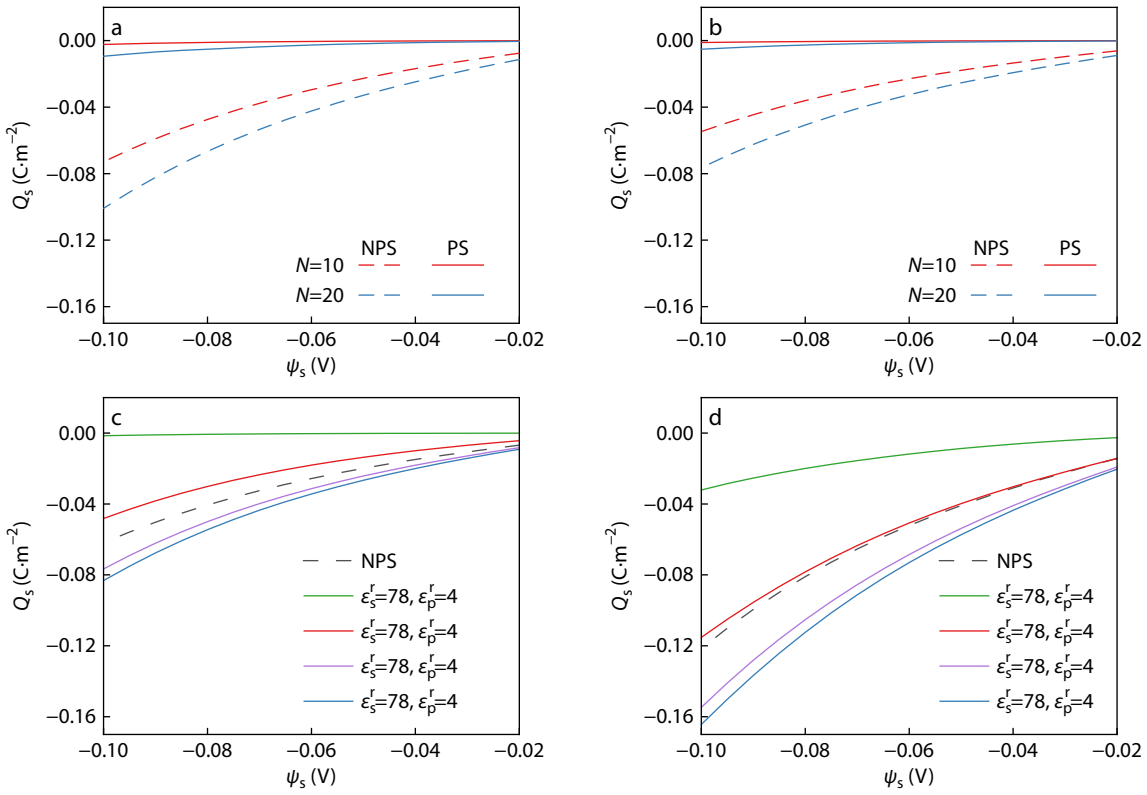

Fig. 3 Surface charge density versus surface potential. The grafting density in (a–c) is $\rho_g = 0.0125\text{nm}^{-2}$ and in (d) is $\rho_g = 0.0625\ \text{nm}^{-2}$. The pore width in (a) is $L = 4$ nm, in (b) is $L = 8$ nm, and in (c, d) is $L = 6$ nm. The chain length in panels (c, d) is $N = 10$.

should be mentioned for electrode with finite permittivity, the electric field inside the electrode also has an important effect on the electrostatic potential. This can be an interesting research topic in the future. Herein, we use the boundary condition of Eq. (38) for the simplicity, because too many factors and parameters have been considered in this work. When the substrate is uncharged, the self-energy effect on the PE brush is weak. When the substrate is charged, this effect is important. The PE brush structure at equilibrium is synergistically regulated by surface electrostatic repulsion, excluded volume effect and ion correlation effects. Owing to the presence of surface charges, the substrate must adsorb additional compensatory counterions to neutralize the surface charges of the substrate.

As ψ_s increases, all the curves in Fig. 3 exhibit a nonlinear concave trend with a gradually increasing slope. This means that the response of charge accumulation to ψ_s is gradually increased owing to the ion rearrangement. When the chain length increases from $N = 10$ to 20, the curves shift downward overall and the slope further increases. This trend indicates that longer chains offer more local immobile charges and form a thicker double-layer region, which in turn leads to stronger ion adsorption or screening effect. Interfacial polarization always yields a lower surface charge density than the NPS case. The difference is most pronounced at high applied potential and for narrow slit, where polarization-induced screening is stronger. As the slit size L increases from 4 nm to 8 nm, the overall surface charge density decreases. This indicates that wider slit weakens the coupling between the applied electric field and interfacial polarization, thereby reducing the interfacial charge accumulation.

As ε_s is fixed and ε_p increases, the $\psi_s - Q_s$ curves move downward with a greater curvature (Fig. 3c). In other words, higher ε_p reduces the counteracting polarization inside the electrode plate, which allows more applied field to penetrate into the solvent and thus promotes ion accumulation at the electrode-electrolyte interface. As a reference, the case $\varepsilon_s = \varepsilon_p$ is considered, for which the dielectric contrast at the interface vanishes. Under this condition, image charge effect is absent. The self-energy contribution arises solely from the entropic effect associated with spatial inhomogeneity of ion densities. Electrodes with a higher dielectric permittivity may also produce a stronger local field-enhancement region, further amplifying the interfacial charge density. With increasing ρ_g, the curves also shift downward. More charges are supplied at higher grafting density. The PE chains are stretched more in z-direction, and the effective interfacial volume is also increased. Consequently, the thickness of counterion layer is increased. These effects synergistically increase the surface charge density.

The energy storage performance of PE-coated SCs can be described by capacitance C and energy density E, which are calculated by

$$C = \frac{Q_s}{\psi_s}, E = \frac{1}{2}C\psi_s^2 \tag{39}$$

For opposing PE brushes confined in slit pore,[68] if the pore width is relatively small, the chain extension would be restricted by the two surfaces. The opposed chains are compressed to contact with each other, which may lead to the

competition between entropic elasticity and electrostatic force.[69]

The $\psi_s - Q_s$ curves give the overall charge response of the system under different grafting conditions. In order to reveal the microscopic mechanism, the density distributions of PE segments and counterions in a slit pore are plotted. Fig. 4 shows the density distributions of PE segments and counterions in a slit pore with a width of 6 nm. As the charge density on the substrate surface increases, the native chain segments tend to move away from the charged surface due to electrostatic repulsion. In addition, for PE coatings, more counterions are introduced into this system in order to ensure the electroneutrality of the whole system. However, the introduction of the self-energy effect significantly weakens the ability of the surface charges to modulate the distribution of the chain segments, leading to smaller differences in the density distribution. This is also attributed to the spatial rearrangement of the counterion cloud that partially shield the long-range electrostatic force generated by the surface charges in salt-free systems. As a result, the short-range correlation becomes the dominant factor.

The density distributions of PE segments and counterions (Fig. 4) directly determine the distributions of electric potential and net charge within the pore (Fig. 5). Meanwhile, the electric potential distribution quantifies the effective amount of charge at the electrode-electrolyte interface, providing a direct physical guide for optimizing the SCs performance by changing grafting conditions. Fig. 5 reveals the key influence of self-energy effect on the electric potential and net charge distribution. The electric potential distribution (Figs. 5a and 5b) is compared with the net charge distribution (Figs. 5c and 5d) in order to directly relate the electric potential pattern to the charge distribution. The solid (PS) and dashed (NPS) lines demonstrate clear differences between the cases of $\psi_s = -0.01$, -0.05 and -0.10 V. The potential inside the pore in the PS case is nearly flat in the z-direction, whereas the NPS exhibits a parabolic curvature with a pronounced bulge towards the midplane. Correspondingly, the net charge of the PS shows a sharper and more concentrated peak close to the solid surface, whereas the NPS exhibits a wider charge distribution accompanied by more pronounced oscillations at the boundaries. Polar plate polarization yields to the shielding effect in the near-surface region by generating image charges that locally reduce the applied field, with ρ_{net} approaching zero.

The energy storage performance is also greatly influenced by the temperature. Fig. 6 illustrates the relationship between surface charge density and potential, as well as its response to temperature and electrode polarization effect. In both cases of PS and NPS, as ψ_s decreases, the driving force for ion adsorption by the electric double layer becomes weak, leading to a reduction in surface charge density. For all the cases, higher temperatures result in lower surface charge densities, because the ion mobility is enhanced. When the polarization effect is considered, all curves shift slightly downwards in high-ψ_s region, indicating that polarization charges induce stronger local electric field in the electrode, thereby enhancing the aggregation effect of counterions. This shift is

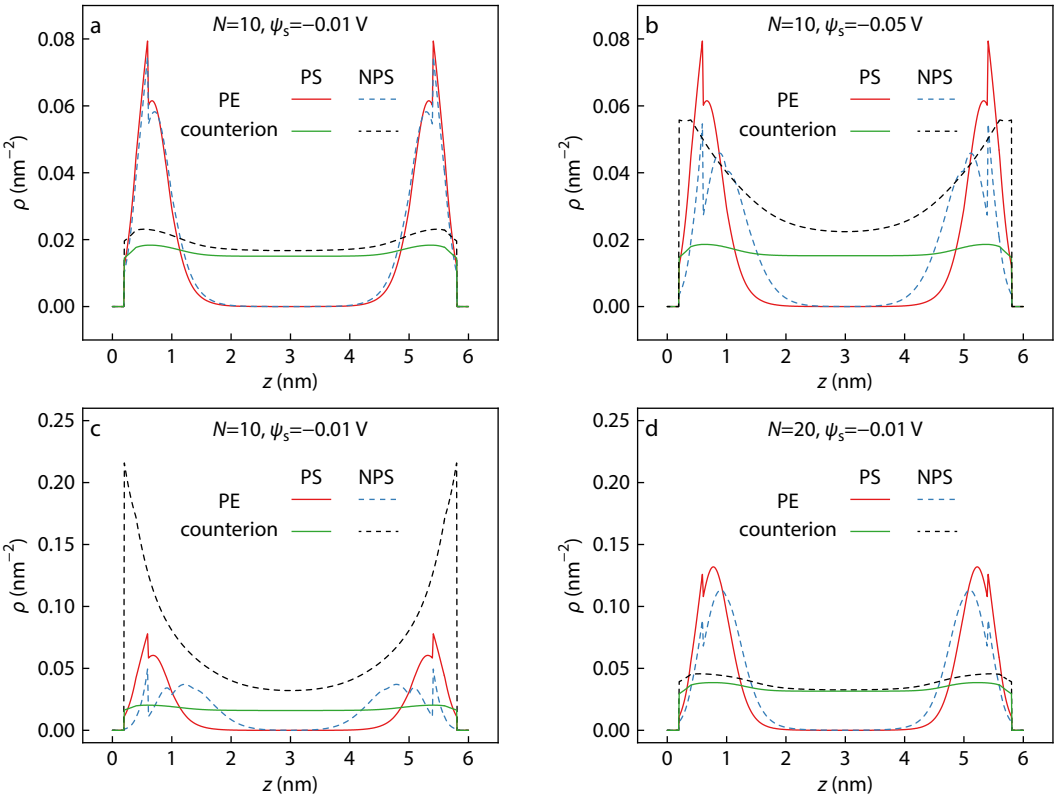

Fig. 4 Density distributions of PE segments and counterions. The grafting density ρ_g=0.0125 nm^{-2}. The pore width L=6 nm. The relative dielectric permittivities of the solvent ε_s^r and substrate ε_p^r are 78 and 4, respectively.

https://doi.org/10.1007/s10118-026-3710-x

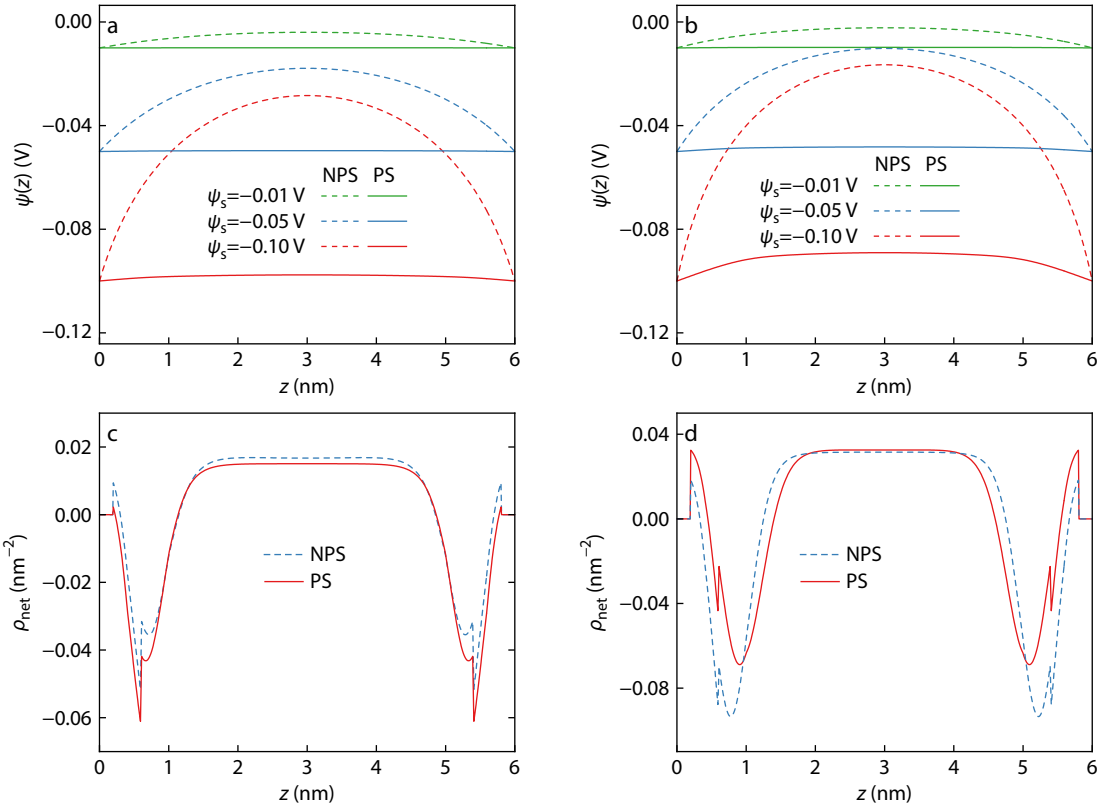

Fig. 5 Electric potential and net charge distribution in the slit pores. The grafting density ρ_g=0.0125 nm^{-2}. The chain lengths of the first and second columns are at 10 and 20, respectively. The relative dielectric permittivities of the solvent ε_s^r and substrate ε_p^r are 78 and 4, respectively.

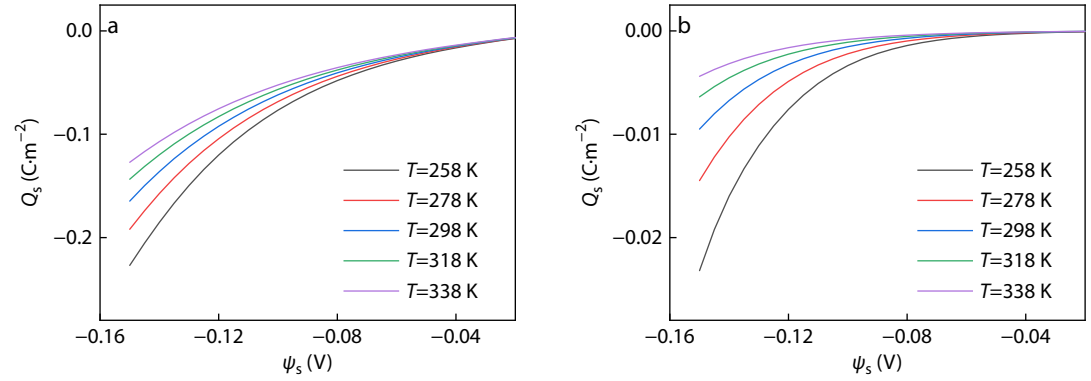

Fig. 6 Surface charge density at different temperatures. The grafting density ρ_g=0.0125 nm^{-2}. The pore width L=6nm. The relative dielectric permittivities of the solvent ε_s^r and substrate ε_p^r are 78 and 4, respectively. (a) NPS case; (b) PS case.

more pronounced at low temperatures and high potentials.

At N=10 and ρ_g=0.0125 nm^{-2}, as ε_p^r increases from 4 to 25 and 100, the PE segment density at the first peak decreases monotonically, while the ion density significantly increases (Fig. 7). It is attributed to the fact that the repulsion of like charges becomes weak as increasing ε_p^r, which promotes the ion enrichment at the electrode-electrolyte interface. The image-charge effect is reduced as increasing the substrate permittivity ε_p^r. More counterions are distributed in the near-wall region. The chain electrostatic repulsion is reduced due to the enhanced local screening effect. As a result, the chains partially collapse. When ρ_g increases, although the overall peak of PE segments decreases and shifts slightly away from the interface, ε_p^r still determines the intensity of ion enrichment in the near-wall region. When the chain length is increased to N=20 at ρ_g=0.0125 nm^{-2}, the high-dielectric substrate similarly induces a more compact ion layer, causing the PE chains to shrink toward the surface. The increase in the dielectric permittivity of the substrate promotes an increase in ion concentration at the electrode-electrolyte interface by reducing the image-charge repulsion.

The energy storage performance of SCs is calculated by varying the grafting conditions. The data are shown in Fig. 8. As ρ_g increases from 0.0125 nm^{-2} to 0.0625 nm^{-2}, both capacitance C and energy density E exhibit a clear monotonic increase, regardless of whether the potential is low (−0.01 V)

https://doi.org/10.1007/s10118-026-3710-x

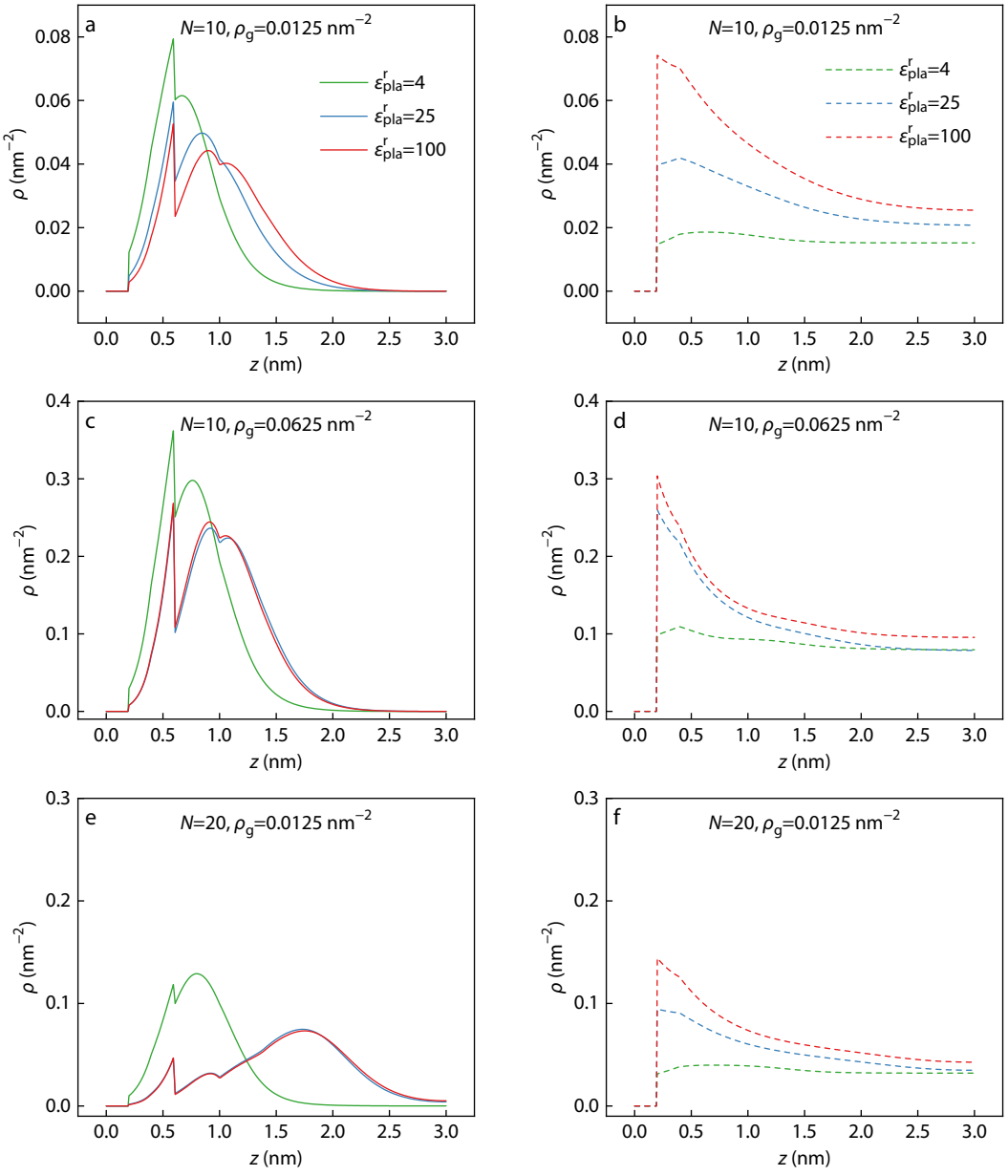

Fig. 7 Effect of substrate dielectric permittivity on the density distribution of PE (first column) and counterions (second column) under different grafting conditions. The pore width L=6 nm. The potential is fixed at −0.05 V.

or high (−0.10 V). That is true for both chain lengths, but the gain from long chains (N=20) is significantly greater than that from short chains (N=10). It indicates that the total charge and spatial distribution of PE chains play an important role in enhancing the double-layer structure. Long chains can attract more counterions and form thicker charged brush layers on the electrode surface, thereby increasing effective charge storage and enhancing the capacitance.

As the surface potential increases from −0.01 V to −0.10 V, the energy density would be amplified at the same capacitance. Therefore, the absolute values of C and E shown in the second column (−0.10 V) are significantly larger than those in the first column. The increasing trend becomes more pronounced with the increase of ρ_g. In addition, at higher surface potentials, the relative contributions of interfacial polarization and image charge effect are strong, explaining why PS/NPS still exhibits differences. It is evident that the capacitance and energy density are enhanced as increasing grafting density or extending the PE chain length. At a low grafting density, electrode polarization significantly suppresses the accumulation of free ions near the double layer, resulting in lower C and E values for PS compared to NPS. At a high grafting density, the excluded volume effect is strong so that the influence of dielectric contrast becomes weak. As a result, the differences for the data between PS and NPS are reduced.

Temperature also has a significant impact on the performance of SCs. The results shown in Fig. 9 indicate that within the temperature range of 258 and 338 K, the capacitance C and energy density E both decrease monotonically with temperatures (Figs. 9a and 9b). Additionally, when the applied

https://doi.org/10.1007/s10118-026-3710-x

potential increases, the corresponding C and E values are significantly higher than those at lower potential, indicating that charge accumulation at the electrode surface plays a dominant role in enhancing the energy storage performance of this system. Specifically, the electrostatic attraction between the electrode and counterions is enhanced as increasing the surface potential. This allows ions to approach the surface more closely and form a more compact interfacial layer. Therefore, the number of charges stored per unit area increases.

Comparing the PS and NPS cases (Figs. 9c and 9d), it can be observed that the capacitance and energy density in the NPS case are generally higher than those in the PS case, particularly under low-temperature conditions. As the temperature increases, the difference gradually decreases and tends to converge. The reason for this phenomenon is the coupled effect of changes in the double-layer structure and dielectric contrast. First, increasing the temperature enhances ion thermal diffusion, thereby suppressing the ion adsorption near the electrode surface and leading to a decrease in double-layer capacitance. Second, in PS cases, the dielectric response within the electrode alters the electric field distribution and induces the image charge effect, typically exerting additional repulsion on free ions near the interface. The accumulated charges in the near-surface region are reduced. Under high screening conditions, the surface polarization effect becomes weak. Furthermore, as the applied potential increases, ion-surface interaction and Coulombic interaction becomes strong, promoting counterions toward the electrode. This leads to a marked increase in C and produces a clear separation between the high-potential and low-potential curves. Simultaneously, the stronger electric field also enhances the electrode polarization response, so PS and NPS maintain a notable difference at high potential but are overall amplified by the electric field.

To investigate the effect of dielectric permittivity on SCs performance, the capacitance and energy density of SCs are calculated by varying the dielectric permittivity of the substrate (Fig. 10). When the substrate dielectric permittivity increases from 4 to 25 and then to 100, the capacitance C shows a significant increasing trend. Furthermore, as the potential increases, the increasing slope in C becomes significantly more pronounced. Specifically, under the condition of −0.10 V, the capacitance jumps from approximately 0 to 0.48 ($\varepsilon_p^r = 25$) and then to 0.83 ($\varepsilon_p^r = 100$), which is much higher than the capacitance at −0.01 and −0.05 V. This phenomenon is primarily attributed to the higher dielectric permittivity of the substrate enhancing the polarization effect at the electrode dielectric interface. Increased interfacial polarization promotes the charge accumulation density within the porous structure. Additionally, the higher applied potential provides a stronger driving field, facilitating the redistribution and adsorption of PE chains and ions within the pore and further enhancing the capacitance. Fig. 10(b) illustrates the

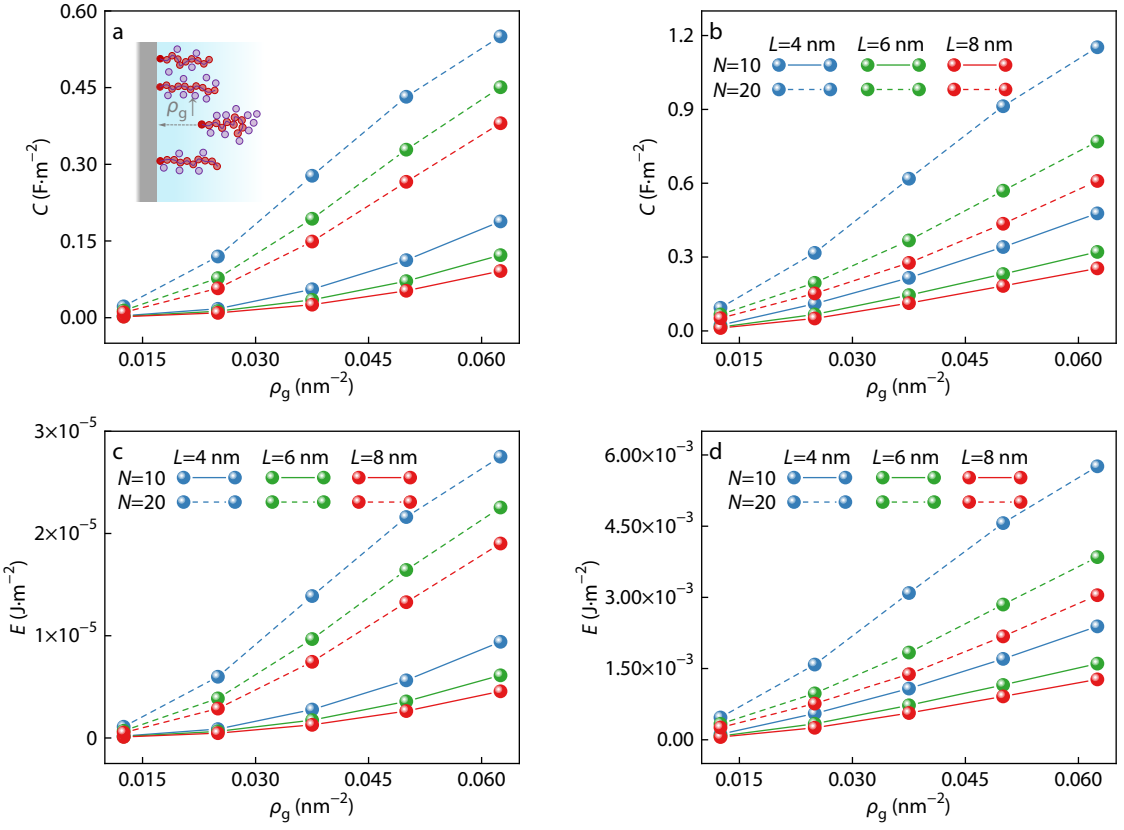

Fig. 8 (a, b) The effect of grafting conditions on the capacitance; (c, d) The effect of grafting conditions on the energy density. The surface potentials in the first and second columns are fixed at −0.01 and −0.10 V, respectively. The relative dielectric permittivities of the solvent ε_s^r and substrate ε_p^r are 78 and 4, respectively.

https://doi.org/10.1007/s10118-026-3710-x

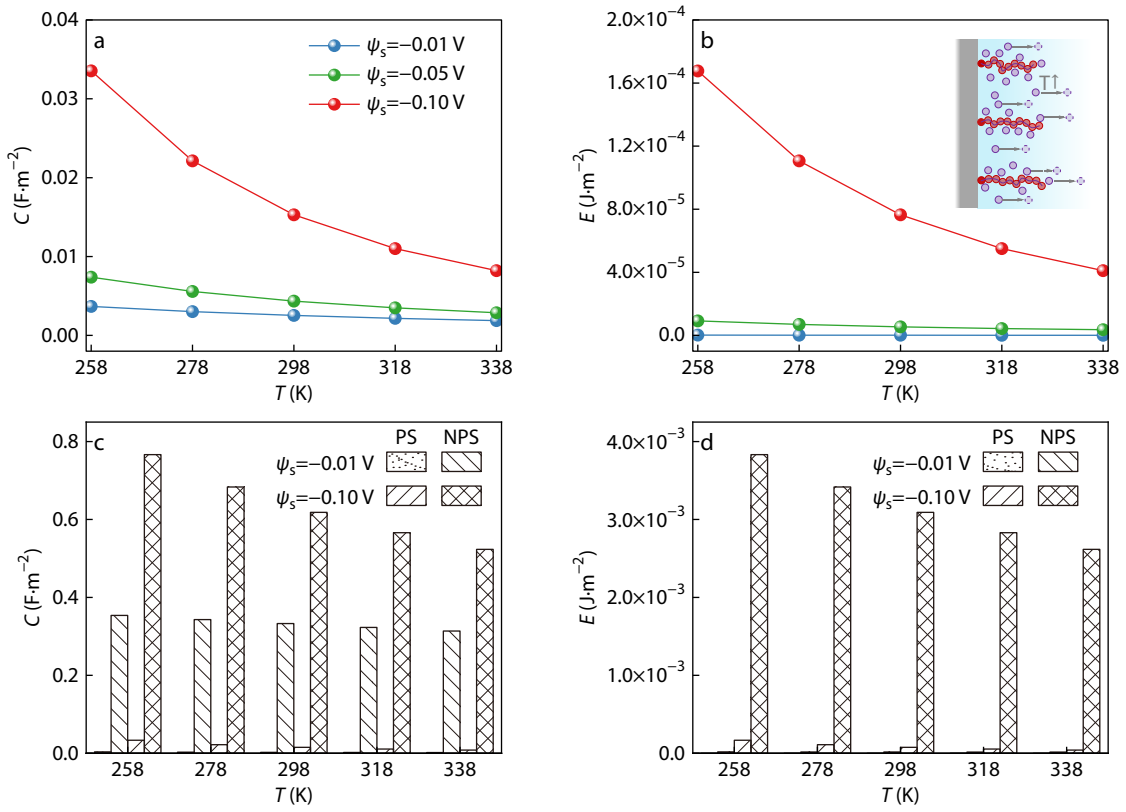

Fig. 9 Effect of temperature on capacitance and energy density: (a, b) in the PS case, (b–d) the comparison between the PS case and the NPS case. The grafting density ρ_g=0.0125nm^{-2}. The pore width L=6nm. The chain length in panels is N=10. The relative dielectric permittivities of the solvent ε_s^r and substrate ε_p^r are 78 and 4, respectively.

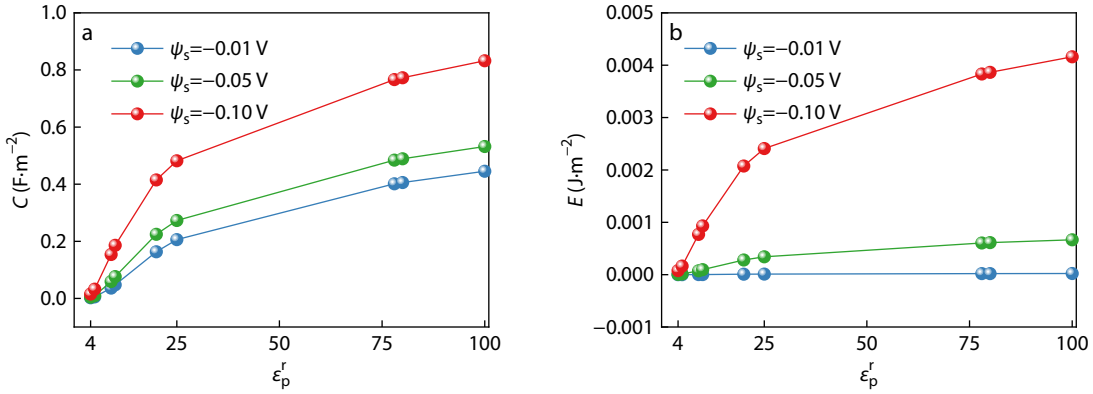

Fig. 10 Effect of substrate dielectric permittivity on the capacitance and energy density. The grafting density ρ_g is fixed at 0.0125 nm^{-2}. The pore width L=6 nm. The chain length in panels is N=10. The relative dielectric permittivity of the substrate ε_s^r=78.

variation in energy density with changes in the substrate dielectric permittivity under the corresponding conditions. The energy density also increases with an increase of substrate dielectric permittivity and potential. The energy storage performance of SCs in microscopic porous double-layer systems can be significantly enhanced by optimizing the dielectric properties of the substrate material and increasing the operating potential.

CONCLUSIONS

The effect of interfacial polarization on the energy storage performance of SCs with PE-grafted electrodes is studied by cDFT, which self-consistently integrates the influences of dielectric contrast, image-charge interaction, and molecular correlation. The systematic theoretical investigation yields several fundamental conclusions. The microstructure of the PE brush layer is a significant factor governing capacitive behavior. Increasing the grafting density and the chain length of the PEs adds more ions to the system and this naturally leads to a significant enhancement in surface charge density, capacitance, and energy density. For long and dense PE chains, the interfacial region is extended, which attracts more counterions near the electrode. It is

https://doi.org/10.1007/s10118-026-3710-x

found that the dielectric contrast between the electrode substrate and the solvent, a factor often oversimplified in idealized models, plays a decisive role. A higher dielectric permittivity of the substrate weakens the shielding effect of the polarization field within the electrode. Consequently, the external electric field provides a stronger influence on the electrolyte, promoting a denser accumulation of counterions at the interface. Crucially, a high-dielectric substrate mitigates the repulsive image-charge interaction near a low-dielectric surface, effectively transforming it into an attractive force that further adsorbs charge near the electrode. The results reveal the interplay between the dielectric properties of the substrate and the structural characteristics of PE brushes in determining the energy storage performance of SCs. These findings also have direct experimental relevance. The predicted ion enrichment and conformational changes of PE chains near high-permittivity substrates can be probed experimentally through techniques such as electrochemical impedance spectroscopy,[70] capacitance measurements,[71] or surface force measurements.[72] The electrostatic properties near the electrode substrates can be regulated to improve energy storage performance. Therefore, the present results provide useful guidance for the design and optimization of electrode materials through dielectric engineering.

Conflict of Interests

The authors declare no interest conflict.

Electronic Supplementary Information

Electronic supplementary information (ESI) is available free of charge in the online version of this article at http://doi.org/10.1007/s10118-026-3710-x.

Data Availability Statement

The data that support the findings of this study are available from the corresponding author upon reasonable request.

ACKNOWLEDGMENTS

This work was financially supported by the Fundamental Research Funds for the Central Universities.

REFERENCES

1 Patel, A.; Patel, S. K.; Singh, R. S.; Patel, R. P. Review on recent advancements in the role of electrolytes and electrode materials on supercapacitor performances. *Discov. Nano* **2024**, *19*, 188.
2 Zhai, Z.; Zhang, L.; Du, T.; Ren, B.; Xu, Y.; Wang, S.; Miao, J.; Liu, Z. A review of carbon materials for supercapacitors. *Mater. Des.* **2022**, *221*, 111017.
3 Kumar, N. A.; Choi, H.-J.; Shin, Y. R.; Chang, D. W.; Dai, L.; Baek, J. B. Polyaniline-grafted reduced graphene oxide for efficient electrochemical supercapacitors. *ACS Nano* **2012**, *6*, 1715−1723.
4 Mazur, D.; Brandyshev, P.; Doronin, S.; Budkov, Y. A. Understanding the electric double layer at the electrode-electrolyte interface: part i - no ion specific adsorption. *ChemPhysChem* **2024**, e202400650.
5 Fumagalli, L.; Esfandiar, A.; Fabregas, R.; Hu, S.; Ares, P.; Janardanan, A.; Yang, Q.; Radha, B.; Taniguchi, T.; Watanabe, K.; Gomila, G.; Novoselov, K. S.; Geim, A. K. Anomalously low dielectric constant of confined water. *Science* **2018**, *360*, 1339−1342.
6 Goldsmith, Z. K.; Secor, M.; Hammes-Schiffer, S. Inhomogeneity of interfacial electric fields at vibrational probes on electrode surfaces. *ACS Cent. Sci.* **2020**, *6*, 304−311.
7 Jeanmairet, G.; Rotenberg, B.; Salanne, M. Microscopic simulations of electrochemical double-layer capacitors. *Chem. Rev.* **2022**, *122*, 10860−10898.
8 Zhou, T.; Bruch, D.; Wang, Z.-G. Image charge effects under metal and dielectric boundary conditions. *Phys. Rev. E* **2024**, *110*, 044129.
9 Wang, Z.; Zhang, W.; Tan, Y.; Liu, Y.; Kong, L.; Kang, L.; Ran, F. Electrolyte-philic electrode material with a functional polymer brush. *ACS Appl. Mater. Interfaces* **2019**, *11*, 16087−16095.
10 Ávila-Niño, J. A.; Olvera, L. I. Ionic self-assembled organogel polyelectrolytes for energy storage applications. *RSC Adv.* **2020**, *10*, 11743−11749.
11 He, X.; Zhang, K.; Li, T.; Jiang, Y.; Yu, P.; Mao, L. Micrometer-scale ion current rectification at polyelectrolyte brush-modified micropipets. *J. Am. Chem. Soc.* **2017**, *139*, 1396−1399.
12 Stehle, P.; Langer, F.; Vrankovic, D.; Anjass, M. Thickness variation of conductive polymer coatings on si anodes for the improved cycling stability in full pouch cells. *ACS Appl. Mater. Interfaces* **2024**, *16*, 27202−27208.
13 Ye, F.; Yang, W.; Liao, X.; Dong, C.; Xu, L.; Mai, L. A micro battery supercapacitor hybrid device with ultrahigh cycle lifespan and power density enabled by bi-functional coating design. *Adv. Funct. Mater.* **2025**, *35*, 2413379.
14 Qin, J. Charge polarization near dielectric interfaces and the multiple-scattering formalism. *Soft Matter* **2019**, *15*, 2125−2134.
15 Becker, M.; Loche, P.; Rezaei, M.; Wolde-Kidan, A.; Uematsu, Y.; Netz, R. R.; Bonthuis, D. J. Multiscale modeling of aqueous electric double layers. *Chem. Rev.* **2024**, *124*, 1−26.
16 Bonthuis, D. J.; Gekle, S.; Netz, R. R. Dielectric profile of interfacial water and its effect on double-layer capacitance. *Phys. Rev. Lett.* **2011**, *107*, 166102.
17 Groß, A.; Sakong, S. Ab initio simulations of water/metal interfaces. *Chem. Rev.* **2022**, *122*, 10746−10776.
18 Curtis, R. A.; Lue, L. Depletion forces due to image charges near dielectric discontinuities. *Curr. Opin. Colloid Interface Sci.* **2015**, *20*, 19−23.
19 Liang, J.; Yuan, J.; Luijten, E.; Xu, Z. Harmonic surface mapping algorithm for molecular dynamics simulations of particle systems with planar dielectric interfaces. *J. Chem. Phys.* **2020**, *152*, 134109.
20 Frydel, D. Polarizable poisson–boltzmann equation: the study of polarizability effects on the structure of a double layer. *J. Chem. Phys.* **2011**, *134*, 234704.
21 Lesniewska, N.; Beaussart, A.; Duval, J. F. L. Electrostatic interactions between soft nanoparticles beyond the derjaguin approximation: effects of finite size of ions and charges, dielectric decrement and ion correlations. *J. Colloid Interface Sci.* **2025**, *678*, 808−827.
22 Nap, R.; Gong, P.; Szleifer, I. Weak polyelectrolytes tethered to surfaces: effect of geometry, acid–base equilibrium and electrical permittivity. *J. Polym. Sci., Part B: Polym. Phys.* **2006**, *44*, 2638−2662.
23 Jiang, T.; Wu, J. Ionic effects in collapse of polyelectrolyte brushes. *J. Phys. Chem. B* **2008**, *112*, 7713−7720.
24 Balzer, C.; Wang, Z.-G. Electroresponse of weak polyelectrolyte brushes. *Eur. Phys. J. E* **2023**, *46*, 82.
25 Zhao, S.; Zhang, P.; Lian, Z. A fast stimuli-responsive brush with

Graphical Abstract

Energy Storage Performance of Supercapacitors with Polyelectrolyte Surface Coatings: Effects of Dielectric Contrast

Yi-Yao Han, Ming-Yu Chen, and Xiao-Fei Xu

East China University of Science and Technology

Classical density functional theory is employed to study the energy storge performance of supercapacitor with polyelectrolyte surface coating. The dielectric contrast effects between the electrode substrate and the solvent are explicitly accounted. It is found that the dielectric contrast plays a decisive role in determining the energy storage performance.

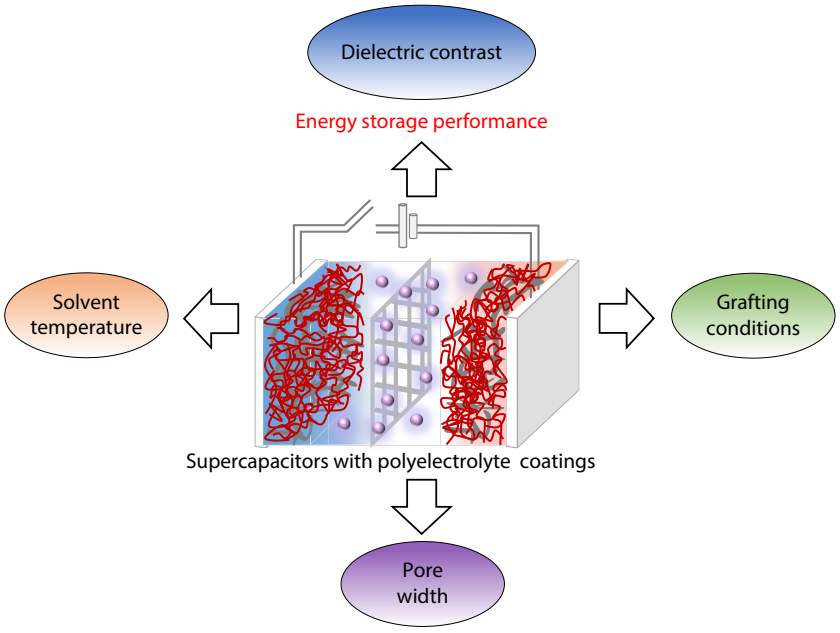

Chinese J. Polym. Sci., 2026 *https://doi.org/10.1007/s10118-026-3710-x*

regulated exposed–adsorbed transition of minority polyelectrolyte chains. *Macromolecules* **2025**, *58*, 8498–8510.
26 Duan, C.; Agrawal, N. R.; Wang, R. Electrostatic correlation augmented self-consistent field theory and its application to polyelectrolyte brushes. *Phys. Rev. Lett.* **2025**, *134*, 048101.
27 Netz, R. R.; Andelman, D. Neutral and charged polymers at interfaces. *Phys. Rep.* **2003**, *380*, 1–95.
28 Qiu, G.; Qiu, Q.; Qing, L.; Zhou, J.; Xu, X.; Zhao, S. Effects of polyelectrolyte surface coating on the energy storage performance in supercapacitors. *J. Phys. Chem. C* **2022**, *126*, 8218–8226.
29 Qing, L.; Jiang, J. Enabling high-capacitance supercapacitors by polyelectrolyte brushes. *ACS Nano* **2023**, *17*, 17122–17130.
30 Li, Z.; Wu, J. Density functional theory for planar electric double layers: closing the gap between simple and polyelectrolytes. *J. Phys. Chem. B* **2006**, *110*, 7473–7484.
31 Jiang, D.; Meng, D.; Wu, J. Density functional theory for differential capacitance of planar electric double layers in ionic liquids. *Chem. Phys. Lett.* **2011**, *504*, 153–158.
32 Feng, J.; Wang, Y.; Xu, Y.; Sun, Y.; Tang, Y.; Yan, X. Ion regulation of ionic liquid electrolytes for supercapacitors. *Energy Environ. Sci.* **2021**, *14*, 2859–2882.
33 Park, J.; Lee, J.; Kim, W. Water-in-salt electrolyte enables ultrafast supercapacitors for ac line filtering. *ACS Energy Lett.* **2021**, *6*, 769–777.
34 Zheng, Q.; Goodwin, Z. A. H.; Gopalakrishnan, V.; Hoane, A. G.; Han, M.; Zhang, R.; Hawthorne, N.; Batteas, J. D.; Gewirth, A. A.; Espinosa-Marzal, R. M. Water in the electrical double layer of ionic liquids on graphene. *ACS Nano* **2023**, *17*, 9347–9360.
35 Shin, S. J.; Kim, D. H.; Bae, G.; Ringe, S.; Choi, H.; Lim, H.-K.; Choi, C. H.; Kim, H. On the importance of the electric double layer structure in aqueous electrocatalysis. *Nat. Commun.* **2022**, *13*, 174.
36 Xu, X. F. Surface polarization effects on collapse transition of polyelectrolyte brushes. *Chinese J. Polym. Sci.* **2024**, *42*, 1313–1320.
37 Chen, M.; Xu, X. Structure of a grafted polyelectrolyte layer at the dielectric interface: coupling effects of dielectric contrast, ionic strength, and excluded volume. *J. Phys. Chem. B* **2025**, *129*, 4595–4604.
38 Wu, Q.; Xu, Y.; Yao, Z.; Liu, A.; Shi, G. Supercapacitors based on flexible graphene/polyaniline nanofiber composite films. *ACS*

Nano **2010**, *4*, 1963−1970.
39 Zhao, Y.; Liu, J.; Hu, Y.; Cheng, H.; Hu, C.; Jiang, C.; Jiang, L.; Cao, A.; Qu, L. Highly compression-tolerant supercapacitor based on polypyrrole-mediated graphene foam electrodes. *Adv. Mater.* **2013**, *25*, 591−595.
40 Wu Jianzhong. Variational methods in molecular modeling. *Springer Singap*. **2017**, *10.1007/978-981-11-2502–0*.
41 Te Vrugt, M.; Löwen, H.; Wittkowski, R. Classical dynamical density functional theory: from fundamentals to applications. *Adv. Phys.* **2020**, *69*, 121−247.
42 Xu, X.; Ting, C. L.; Kusaka, I.; Wang, Z.-G. Nucleation in polymers and soft matter. *Annu. Rev. Phys. Chem.* **2014**, *65*, 449−475.
43 Wu, J. Understanding the electric double-layer structure, capacitance, and charging dynamics. *Chem. Rev.* **2022**, *122*, 10821−10859.
44 Xu, X.; Cao, D.; Wu, J. Density functional theory for predicting polymeric forces against surface fouling. *Soft Matter* **2010**, *6*, 4631.
45 Xu, X.; Cao, D. Density functional theory for adsorption of colloids on the polymer-tethered surfaces: effect of polymer chain architecture. *J. Chem. Phys.* **2009**, *130*, 164901.
46 Yu, Y.-X.; Wu, J. Structures of hard-sphere fluids from a modified fundamental-measure theory. *J. Chem. Phys.* **2002**, *117*, 10156−10164.
47 Rosenfeld, Y. Free-energy model for the inhomogeneous hard-sphere fluid mixture and density-functional theory of freezing. *Phys. Rev. Lett.* **1989**, *63*, 980−983.
48 Roth, R.; Evans, R.; Lang, A.; Kahl, G. Fundamental measure theory for hard-sphere mixtures revisited: the white bear version. *J. Phys. Condens. Matter* **2002**, *14*, 12063−12078.
49 Jiang, J.; Liu, H.; Hu, Y.; Prausnitz, J. M. A molecular-thermodynamic model for polyelectrolyte solutions. *J. Chem. Phys.* **1998**, *108*, 780−784.
50 Jiang, J. W.; Blum, L.; Bernard, O.; Prausnitz, J. M. Thermodynamic properties and phase equilibria of charged hard sphere chain model for polyelectrolyte solutions. *Mol. Phys.* **2001**, *99*, 1121−1128.
51 Yu, Y.-X.; Wu, J. Density functional theory for inhomogeneous mixtures of polymeric fluids. *J. Chem. Phys.* **2002**, *117*, 2368−2376.
52 Wertheim, M. S. Fluids with highly directional attractive forces. iii. multiple attraction sites. *J. Stat. Phys.* **1986**, *42*, 459−476.
53 Wertheim, M. S. Fluids with highly directional attractive forces. IV. Equilibrium polymerization. *J. Stat. Phys.* **1986**, *42*, 477−492.
54 Waisman, E.; Lebowitz, J. L. Mean spherical model integral equation for charged hard spheres. ii. results. *J. Chem. Phys.* **1972**, *56*, 3093−3099.
55 Blum, L. Mean spherical model for asymmetric electrolytes: I. Method of solution. *Mol. Phys.* **1975**, *30*, 1529−1535.
56 Blum, L.; Hoeye, J. S. Mean spherical model for asymmetric electrolytes. 2. Thermodynamic properties and the pair correlation function. *J. Phys. Chem.* **1977**, *81*, 1311−1316.
57 Jiang, J.; Gillespie, D. Revisiting the charged shell model: a density functional theory for electrolytes. *J. Chem. Theory Comput.* **2021**, *17*, 2409−2416.
58 Wu, J.; Jiang, T.; Jiang, D.; Jin, Z.; Henderson, D. A classical density functional theory for interfacial layering of ionic liquids. *Soft Matter* **2011**, *7*, 11222.
59 Xu, X.; Qiu, Q.; Lu, C.; Zhao, S. Responsive properties of grafted polyanion chains: effects of dispersion interaction and salt. *J. Chem. Eng. Data* **2020**, *65*, 5708−5717.
60 Wang, Z. G. Fluctuation in electrolyte solutions: the self energy. *Phys. Rev. E* **2010**, *81*, 021501.
61 Wang, R.; Wang, Z. G. Effects of image charges on double layer structure and forces. *J. Chem. Phys.* **2013**, *139*, 124702.
62 Wang, R. Effects of self energy of the ions on the double layer structure and properties at the dielectric interface. California Institute of Techology. **2015**, Ph.D Thesis.
63 Netz, R. R. Polyelectrolytes in electric fields. *J. Phys. Chem. B* **2003**, *107*, 8208−8217.
64 Xu, X.; Tang, W.; Gao, Q.; Qiao, C.; Peng, Y.; Zhao, S. Explaining thermodynamic potential to undergraduates. *J. Chem. Educ.* **2024**, *101*, 4714−4721.
65 Stierle, R.; Sauer, E.; Eller, J.; Theiss, M.; Rehner, P.; Ackermann, P.; Gross, J. Guide to efficient solution of pc-saft classical density functional theory in various coordinate systems using fast fourier and similar transforms. *Fluid Phase Equilibria* **2020**, *504*, 112306.
66 Petsev, D. N.; van Swol, F.; Frink, L. J. D. *Molecular theory of electric double layers*; IOP Publishing, **2021**, 2053−2563.
67 Griffiths, D. J. *Introduction to electrodynamics*, 3rd Ed.; New Jersey: Prentice Hall, Inc., **1999**; p. 90.
68 Podgornik, R. Self-consistent-field theory for confined polyelectrolyte chains. *J. Phys. Chem.* **1992**, *96*, 884−896.
69 Zhao, B.; Zhu, L. Nanoscale phase separation in mixed poly(*tert*-butyl acrylate)/polystyrene brushes on silica nanoparticles under equilibrium melt conditions. *J. Am. Chem. Soc.* **2006**, *128*, 4574−4575.
70 Zhou, F.; Hu, H.; Yu, B.; Osborne, V. L.; Huck, W. T. S.; Liu, W. Probing the responsive behavior of polyelectrolyte brushes using electrochemical impedance spectroscopy. *Anal. Chem.* **2007**, *79*, 176−182.
71 Rud, O.; Chertopalov, S.; Borisov, O. Charge storage mechanisms in redox-active polymer brushes. *Macromolecules* **2026**, *59*, 2489−2499.
72 Willott, J. D.; Murdoch, T. J.; Webber, G. B.; Wanless, E. J. Nature of the specific anion response of a hydrophobic weak polyelectrolyte brush revealed by AFM force measurements. *Macromolecules* **2016**, *49*, 2327−2338.